electronics

MDPI

Article

Low-Complexity Model Predictive Control for Series-Winding PMSM with Extended Voltage Vectors

Jinde Hu [1], Zhaoyang Fu [1,2,*], Rongwei Xu [1], Tian Jin [3], Zhengyang Feng [4] and Sheng Wang [3,*]

[1] School of Automation, Northwestern Polytechnical University, Xi'an 710000, China; hujinde@mail.nwpu.edu.cn (J.H.); xurongwei@mail.nwpu.edu.cn (R.X.)
[2] Research & Development Institute, Northwestern Polytechnical University, Shenzhen 518000, China
[3] School of Engineering, Cardiff University, Cardiff CF24 3AA, UK; jint5@cardiff.ac.uk
[4] Toshiba Europe Ltd., 30 Queen Square, Bristol BS1 4ND, UK; jenny.feng@toshiba-bril.com
* Correspondence: fuzy@nwpu.edu.cn (Z.F.); wangs9@cardiff.ac.uk (S.W.)

Abstract: This paper proposes a low-complexity model predictive current control (MPCC) strategy based on extended voltage vectors to enhance the computational efficiency and steady-state performance of three-phase series-winding permanent magnet synchronous motors (TPSW-PMSMs). Compared to conventional MPCC methods, this approach increases the number of candidate voltage vectors in the alpha–beta plane from 8 to 38, thereby achieving better steady-state performance. Specifically, the proposed method reduces the total harmonic distortion (THD) by 59%. To improve computational efficiency, a two-stage filtering strategy is employed, significantly reducing the computational burden. The number of voltage vectors traversed in one control period is reduced from 38 to a maximum of 4, achieving an 89% reduction in traversals. Additionally, to mitigate the impact of zero-sequence currents, zero-sequence current suppression is implemented within the control system for effective compensation. By combining low computational complexity, reliable steady-state performance, and real-time control capabilities, this strategy provides an efficient solution for TPSW-PMSM systems. Simulation results validate the effectiveness of the proposed method.

Keywords: model predictive control (MPC); permanent magnet synchronous motors (PMSM); series-winding topology; low computational burden

check for updates

Academic Editor: Maciej Ławryńczuk

Received: 20 November 2024
Revised: 27 December 2024
Accepted: 30 December 2024
Published: 31 December 2024

Citation: Hu, J.; Fu, Z.; Xu, R.; Jin, T.; Feng, Z.; Wang, S. Low-Complexity Model Predictive Control for Series-Winding PMSM with Extended Voltage Vectors. *Electronics* **2025**, *14*, 127. https://doi.org/10.3390/electronics14010127

Copyright: © 2024 by the authors. Licensee MDPI, Basel, Switzerland. This article is an open access article distributed under the terms and conditions of the Creative Commons Attribution (CC BY) license (https://creativecommons.org/licenses/by/4.0/).

1. Introduction

Permanent magnet synchronous motors (PMSMs) are widely used in industrial applications due to their simple structure, high power density, and efficiency [1]. These features make PMSMs ideal for electric vehicles (EVs), industrial applications, and wind power generation, where energy efficiency and reliability are essential [2–5]. Conventional star-connected motor drive systems typically achieve only 57.7% DC voltage utilization. To overcome this, open-end winding motor drive systems have been extensively studied, proving effective in enhancing DC voltage utilization and improving energy efficiency [6]. Open-end winding motor configurations not only improve voltage utilization but also enhance fault tolerance, making them ideal for critical applications like electric transportation [7–9]. The ability to operate under fault conditions without significant performance degradation enhances the reliability and safety of electric vehicles, electric buses, and other transport systems, which are expected to maintain continuous operation even under challenging conditions [10]. The combination of better voltage efficiency and fault tolerance has driven research into advanced control strategies for open-winding PMSMs to

optimize their practical applications [11]. The introduction of open-end winding topology improves performance but increases system costs due to the use of more power components. Series-winding motor drives offer a cost-effective alternative, balancing performance and cost [12,13]. Compared to open-end winding motor drives, series-winding motor drives achieve the same dc-link utilization. Improved dc-link utilization in AC drive systems offers several benefits: lower voltage limits make it easier to meet battery and isolation requirements [14], and the reduction in bus voltage helps minimize dead-time harmonics [15]. Additionally, this topology only adds a single bridge arm compared to conventional motor drives.

In open-winding and series-winding motor drives, the open neutral point creates a zero-sequence subspace, leading to increased zero-sequence current, higher total harmonic distortion (THD), and greater torque ripple [16–18]. To improve control system performance, suppressing zero-sequence current is essential. Many studies have focused on this issue, especially for open-winding and series-winding motor drives. In Ref. [19], a zero-sequence current suppression method for open-winding motor drive systems is proposed, employing feedforward voltage compensation and a resonant controller to effectively mitigate zero-sequence current. A novel zero-sequence current suppression control strategy designed for a five-phase open-end winding fault-tolerant drive system is proposed [20], utilizing an unequal distribution of zero-voltage vectors for effective suppression. In Ref. [21], a suppression method based on a second-order generalized integrator is introduced, applicable to permanent magnet brushless motor drive systems. Ref. [22] presented a direct torque control strategy for series-winding permanent magnet synchronous motors with zero-sequence current suppression capability. This strategy uses closed-loop control to simultaneously regulate electromagnetic torque, stator flux linkage, and zero-sequence current. In Ref. [23], the authors propose a q-axis current injection method based on angle-shifted voltage distribution to suppress torque ripple. This method effectively counteracts the torque ripple caused by zero-sequence currents by generating a torque component through the injected q-axis current. Based on the above discussion, it can be seen that the active control of zero-sequence currents is necessary for zero-sequence current suppression in the TPSW-PMSM drive [24].

Additionally, model predictive control (MPC), as an advanced control method, has been introduced in TPSW-PMSM drive systems due to its simplicity and flexibility in handling multiple objectives, such as switching frequency, harmonic current suppression, and common-mode voltage elimination [25]. Depending on the control actions, the model predictive control (MPC) strategies for permanent magnet synchronous motors (PMSMs) can be classified into two types: finite control set model predictive control (FCS-MPC) [26,27] and continuous control set model predictive control (CCS-MPC) [28,29]. Due to the computational limitations of microprocessors, CCS-MPC has not seen widespread use, whereas FCS-MPC is more commonly preferred for practical applications [30,31]. FCS-MPC provides simpler computational realization, making it suitable for systems where fast dynamic response is essential and computational resources are limited [32]. Based on different control objectives, MPC for PMSM can be further divided into model predictive current control (MPCC) [33–35], model predictive torque control (MPTC) [36,37], and model predictive speed control (MPSC) [38,39]. The basic principle of conventional MPC involves traversing all possible voltage vectors generated by the converter and selecting the voltage vector that minimizes the cost function as the output. Conventional MPC outputs only one voltage vector per sampling period, which can lead to significant current ripples [40]. To address this issue, duty-cycle-based MPC [41] was proposed, which allocates time between active and null voltage vectors within one period, effectively improving the quality of the output current. However, duty cycle control does not achieve the optimal voltage vector, as the

combination of active and null voltage vectors can only change the magnitude of the basic voltage vector without altering its angle. To address this limitation, multi-vector model predictive control (MV-MPC) [42] was proposed. In this approach, the second vector is not restricted to null vectors but can be selected from all available vectors. Compared to duty ratio model predictive control, MV-MPC significantly improves control performance. It is noteworthy that as the number of secondary voltage vectors increases, the number of voltage vectors that need to be evaluated within one control cycle also rises. This inevitably leads to a greater computational burden, which can affect the real-time performance of the control system.

To this end, a low-complexity model predictive current control with zero-sequence current suppression capability is proposed for the TPSW-PMSM drive system. By subdividing the voltage vectors and pre-combining them, additional virtual voltage vectors are created to improve the system's steady-state performance. At the same time, to reduce the computational burden caused by the increased number of virtual voltage vectors, a simplified search strategy is introduced. This strategy selects the sector in advance based on the location of the reference voltage vector and eliminates redundant voltage vectors by assessing the magnitude of the reference voltage vector, significantly reducing the computational load. Furthermore, to suppress zero-sequence current, the method of zero-sequence voltage injection is employed.

The paper is organized as follows: Section 2 presents the TPSW-PMSM mathematical model and the distribution of basic voltage vectors. Section 3 introduces the simplified sector selection method and voltage distribution principles. Section 4 discusses zero-sequence voltage injection and time allocation for voltage components. Finally, Section 5 presents simulation results to validate the proposed method.

2. Modeling of TPSW-PMSM Drive

2.1. Mathematical Model of the TPSW-PMSM

In Figure 1, three different topologies are presented. Figure 1a illustrates the three-bridge-arm drive structure, which uses the fewest transistors. However, due to its limited output capability, the utilization of the dc-link is restricted to only 57.7%. Figure 1b shows the six-bridge-arm open-winding drive structure, which allows for a 100% utilization of the dc-link, but with a significant increase in the number of transistors. Figure 1c depicts the series-winding drive structure, where the dc-link utilization is the same as that of the open-winding topology, but with only four bridge arms, resulting in a noticeable reduction in the number of transistors.

According to the Clarke and Park transformation, the stator voltage in the d-q-0 coordinate system can be expressed by the following voltage equations:

$$\begin{bmatrix} u_d \\ u_q \\ u_0 \end{bmatrix} = R_s \begin{bmatrix} i_d \\ i_q \\ i_0 \end{bmatrix} + L_{dq0} \frac{d}{dt} \begin{bmatrix} i_d \\ i_q \\ i_0 \end{bmatrix} + \omega_e \begin{bmatrix} -L_q i_q \\ L_d i_d + \psi_f \\ -3\psi_{f3} \sin(3\theta_e) \end{bmatrix} \tag{1}$$

In this context, u_d, u_q, u_0 and i_d, i_q, i_0 represent the voltage and current in the $d-q-0$ coordinate system, respectively. ψ_f denotes the stator flux linkage. ψ_{f3} indicates the third-harmonic rotor flux linkage. R_s represents the stator resistance. θ_e stands for the electrical angle of the rotor. The inductance in the $d-q-0$ axis can be expressed as L_{dq0}. The torque equation of the TPSW-PMSM can be expressed as follows:

$$T_e = \frac{3}{2} n_p [\psi_f i_q + (L_d - L_q) i_d i_q - 6\psi_{f3} \sin(3\theta_e) i_0] \tag{2}$$

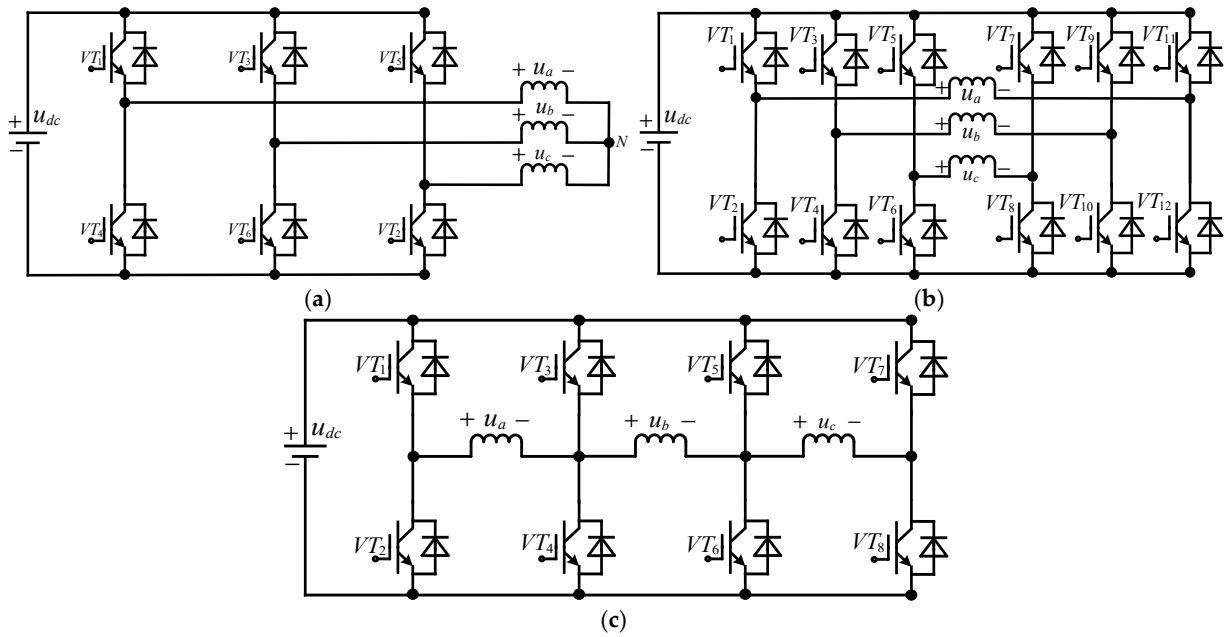

Figure 1. (**a**) Conventional PMSM drive topology diagram; (**b**) TPOW-PMSM drive topology diagram; (**c**) TPSW-PMSM drive topology diagram.

2.2. Voltage Vector Distribution Within the Subspace

Compared to the conventional Y-connected topology, the unique structure of the TPSW-PMSM results in a higher-dimensional zero-sequence subspace and an increased number of basic voltage vectors. Figure 2a shows the three-dimensional distribution of these voltage vectors, while Figure 2b illustrates their two-dimensional distribution. Notably, V_0 and V_{15} are two null voltage vectors that are not shown in the figures.

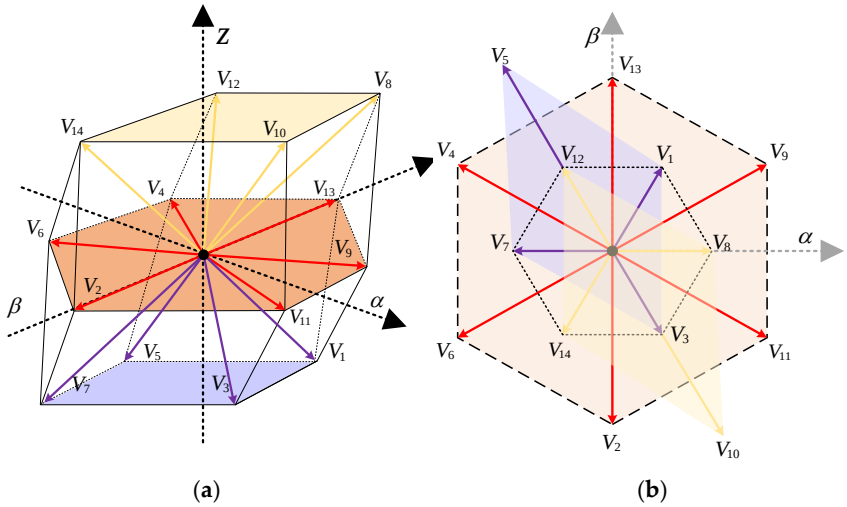

Figure 2. (**a**) Basic voltage vector distribution in 3-D space. (**b**) Basic voltage vector distribution in 2-D space.

To simplify further analysis, Table 1 presents the components of all basic voltage vectors on the $\alpha\beta z$ axis and their corresponding switching states. In the series-winding drive, besides the voltage vectors in the $\alpha\beta$ plane, there are also voltage vectors along the z-axis. As the number of bridge arms increases, the number of voltage vectors grows from the original 2^3 to 2^4. Since the optimal voltage vector in model predictive control (MPC) is selected through an exhaustive search, the increase in voltage vectors inevitably results in

higher computational demands. Out of the 16 basic voltage vectors, V_0 and V_{15} are null vectors that only alter the magnitude of the synthesized voltage vector without changing its angle. The $V_{2,4,6,9,11,13}$ vectors are effective vectors without zero-sequence components, while the vectors $V_{8,10,12,14}$ have positive zero-sequence components with an amplitude of $u_{dc}/3$. Finally, the vectors $V_{1,3,5,7}$ have negative zero-sequence components, with an amplitude of $-u_{dc}/3$.

Table 1. Components of voltage vectors in $\alpha\beta z$ axis.

Voltage Vectors	Switching States	u_α	u_β	u_z
V_0	0000	0	0	0
V_1	0001	$u_{dc}/3$	$u_{dc}/\sqrt{3}$	$-u_{dc}/3$
V_2	0010	0	$-2u_{dc}/\sqrt{3}$	0
V_3	0011	$u_{dc}/3$	$-u_{dc}/\sqrt{3}$	$-u_{dc}/3$
V_4	0100	$-u_{dc}$	$u_{dc}/\sqrt{3}$	0
V_5	0101	$-2u_{dc}/3$	$2u_{dc}/\sqrt{3}$	$-u_{dc}/3$
V_6	0110	$-u_{dc}$	$-u_{dc}/\sqrt{3}$	0
V_7	0111	$-2u_{dc}/3$	0	$-u_{dc}/3$
V_8	1000	$2u_{dc}/3$	0	$u_{dc}/3$
V_9	1001	u_{dc}	$u_{dc}/\sqrt{3}$	0
V_{10}	1010	$2u_{dc}/3$	$-2u_{dc}/\sqrt{3}$	$u_{dc}/3$
V_{11}	1011	u_{dc}	$-u_{dc}/\sqrt{3}$	0
V_{12}	1100	$-u_{dc}/3$	$u_{dc}/\sqrt{3}$	$u_{dc}/3$
V_{13}	1101	0	$2u_{dc}/\sqrt{3}$	0
V_{14}	1110	$-u_{dc}/3$	$-u_{dc}/\sqrt{3}$	$u_{dc}/3$
V_{15}	1111	0	0	0

3. Improved MPCC for TPSW-PMSM

This section presents the improved model predictive current control (MPCC) for TPSW-PMSM, starting with a detailed explanation of its underlying principles and the corresponding mathematical model. The limitations of the conventional MPCC approach are then discussed, leading to the introduction of the proposed improvements in this work.

3.1. Basic Principles of MPCC

First, the discrete mathematical model of the TPSW-PMSM is defined, which is the key to implementing MPCC, as shown in (3).

$$\begin{aligned}\begin{bmatrix} i_d(k+1) \\ i_q(k+1) \\ i_0(k+1) \end{bmatrix} &= \begin{bmatrix} 1-\frac{T_sR_s}{L_d} & \frac{\omega_e T_s L_q}{L_d} & 0 \\ -\frac{\omega_e T_s L_q}{L_q} & 1-\frac{T_sR_s}{L_q} & 0 \\ 0 & 0 & 1-\frac{T_sR_s}{L_0} \end{bmatrix} \begin{bmatrix} i_d(k) \\ i_q(k) \\ i_0(k) \end{bmatrix} \\ &+T_s \begin{bmatrix} u_d(k)/L_d \\ u_q(k)/L_q \\ u_0(k)/L_0 \end{bmatrix} + \omega_e(k) \begin{bmatrix} 0 \\ -T_s\psi_f/L_q \\ 3\psi_{f3}\sin(3\theta_e)T_s/L_0 \end{bmatrix}\end{aligned} \tag{3}$$

k represents the kth step, while $k+1$ denotes the predicted value at the next time step. T_s is the sampling period. The basic principle of MPCC is to utilize the controlled model described above, iteratively traversing all basic voltage vectors during each sampling period to predict future system behavior. The predicted current values are then substituted into the cost function (4) to evaluate errors.

$$g = [i_d^{ref} - i_d(k+1)]^2 + [i_q^{ref} - i_q(k+1)]^2 + \delta[i_0^{ref} + i_0(k+1)]^2 \tag{4}$$

In (4), i_d^{ref}, i_q^{ref}, and i_0^{ref} represent the reference current values. Since the error between i_0 and its reference value is smaller compared to the errors between $i_{d,q}$ and their respective reference values, a weighting coefficient δ is introduced to prioritize i_0 in the control system. The MPCC model selects the voltage vector that minimizes the cost function as the output and applies it within the control period. It is worth noting that due to inherent time delays in system computation and execution, discrepancies may arise between the control signals and system response. To effectively address this issue, a delay compensation component is integrated into the MPCC.

As mentioned in the previous section, the introduction of the zero-sequence subspace generates more voltage vectors, which results in a greater computational burden. This increased complexity can have negative impacts in scenarios where high dynamic performance is required, making the reduction in computational complexity an urgent issue to address. Additionally, in conventional MPCC, only one voltage vector is output per sampling period, which can lead to significant discrepancies between the optimal voltage vector and the desired voltage vector, thereby causing large steady-state errors.

3.2. Basic Principles of Proposed MPCC

As mentioned above, this paper primarily focuses on two aspects of conventional MPCC: computational complexity and steady-state performance. The following sections introduce the methods adopted in this paper for addressing these issues.

3.2.1. Expanded Voltage Vectors

In conventional MPCC, only one voltage vector is output per sampling period, which inevitably results in significant current and torque fluctuations. To address this issue, a duty cycle control (DCC) method is proposed, combining effective voltage vectors (V_2, V_4, V_6, V_9, V_{11}, V_{13}) and null voltage vectors (V_0, V_{15}). This method adjusts the amplitude of the effective voltage vectors to make the final output voltage vector more closely approximate the reference voltage vector. However, since this approach only modifies the amplitude of the voltage vectors, the improvement in steady-state performance is quite limited. Subsequently, a dual-vector model predictive control method (DVMPCC) is introduced, where the selection of the second vector is no longer restricted to null voltage vectors but includes all voltage vectors. This significantly enhances the steady-state performance of the control system. The trade-off, however, is the increased computational burden due to the complex voltage vector traversal and time allocation calculations.

To this end, this section proposes a voltage vector refinement strategy. To address the issue of limited voltage vectors in the $\alpha\beta$ plane, the six original voltage vectors are first divided into three regions based on their magnitudes, as illustrated geometrically in Figure 3a. Compared to conventional MPCC, this approach provides more selectable voltage vectors, resulting in improved steady-state performance. Unlike DCC-MPCC and DV-MPCC, this method eliminates the step of calculating time allocation, thereby reducing computational complexity; however, it requires pre-combination of virtual voltage vectors. An example illustrating the pre-combination principle for any given region is shown in Figure 3b. After the voltage vector subdivision, the 8 effective voltage vectors on the plane expand to 38 vectors. Whether considered from the perspective of vector angles or magnitudes, the refined set of 38 voltage vectors offers a more comprehensive coverage. However, it is important to note that the number of voltage vectors that need to be traversed per cycle increases approximately sixfold. Therefore, it is necessary to pre-filter certain voltage vectors based on the position and magnitude of the reference voltage vector.

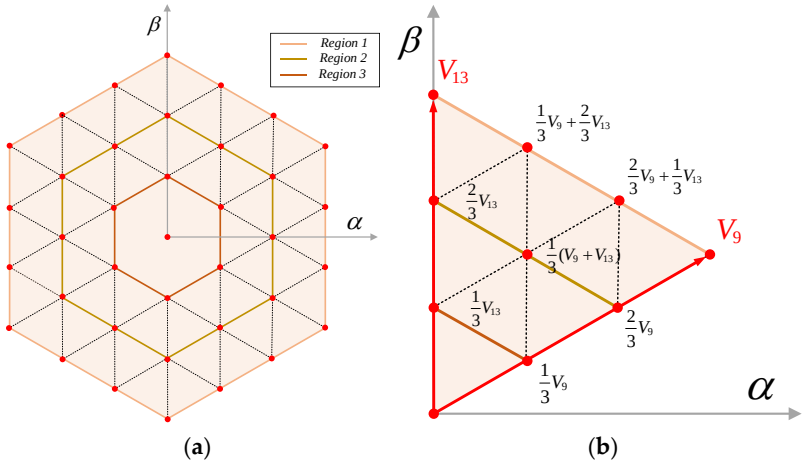

Figure 3. (**a**) Regional subdivision principle. (**b**) Pre-combination principle.

3.2.2. Simplified Voltage Vector Selection

In conventional MPCC, the general method for determining the sector in which the reference voltage lies involves transforming the reference voltage vector obtained from (5) using the inverse Park transformation (6) to obtain its components on the $\alpha\beta$-axis. By dividing these components and calculating the arctangent (7), the angle θ relative to the $\alpha-$ axis is determined, which is then used to identify the sector. Although many microcontroller unit (MCU) manufacturers provide computational libraries that include arctangent functions, these calculations are time-consuming and affect the response speed of the current loop.

$$\begin{cases} u_d^{ref} = R_s i_d(k) + \frac{L_d[i_d^{ref} - i_d(k)]}{T_s} - \omega_e(k) L_q i_q(k) \\ u_q^{ref} = R_s i_q(k) + \frac{L_d[i_q^{ref} - i_q(k)]}{T_s} - \omega_e(k)[L_d i_d(k) + \psi_f] \end{cases} \tag{5}$$

$$\begin{bmatrix} u_\alpha^{ref} \\ u_\beta^{ref} \end{bmatrix} = \begin{bmatrix} \cos\theta_e & -\sin\theta_e \\ \sin\theta_e & \cos\theta_e \end{bmatrix} \begin{bmatrix} u_d^{ref} \\ u_q^{ref} \end{bmatrix} \tag{6}$$

$$\theta = \arctan\left(\frac{u_\alpha^{ref}}{u_\beta^{ref}}\right) \tag{7}$$

Figure 4 illustrates the simplified sector selection principle. First, the (a, b, c) three-phase reference frame is established, with the three axes separated by 120 degrees and perpendicular to the boundaries of sectors I, III, and V, respectively. Therefore, the components u_a, u_b, u_c and u_α, u_β have a clear geometric relationship, as shown in (8). The sector of the reference voltage can be determined based on the polarity of the voltage in the (a, b, c) coordinate system, resulting in $\begin{cases} [\delta_n = 1] \Leftrightarrow [u_x > 0] \\ [\delta_n = 0] \Leftrightarrow [u_x \leq 0] \end{cases}$.

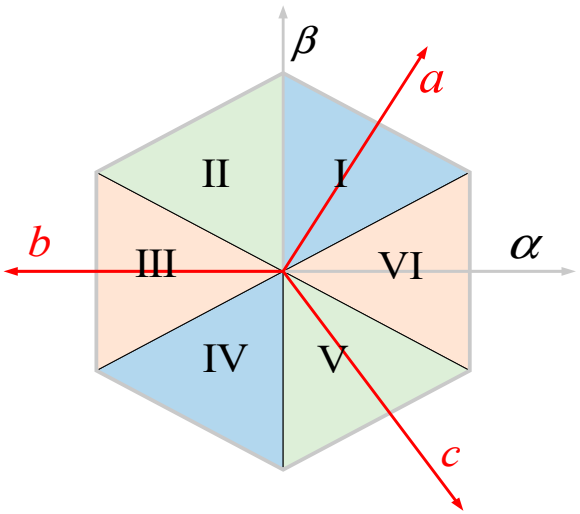

Figure 4. Simplified sector selection principle.

The correspondence between the signs of the components and the sectors is shown in Table 2.

$$\begin{bmatrix} u_a \\ u_b \\ u_c \end{bmatrix} = \begin{bmatrix} \frac{1}{2} & \frac{\sqrt{3}}{2} \\ -1 & 0 \\ \frac{1}{2} & -\frac{\sqrt{3}}{2} \end{bmatrix} \begin{bmatrix} u_\alpha \\ u_\beta \end{bmatrix} \tag{8}$$

Table 2. The relationship between logical variables and the polarity of auxiliary variables.

Sector	Logical Values
I	$\zeta_a\overline{\zeta_b}\overline{\zeta_c}$
II	$\zeta_a\zeta_b\overline{\zeta_c}$
III	$\overline{\zeta_a}\zeta_b\overline{\zeta_c}$
IV	$\overline{\zeta_a}\zeta_b\zeta_c$
V	$\overline{\zeta_a}\overline{\zeta_b}\zeta_c$
VI	$\zeta_a\overline{\zeta_b}\zeta_c$

After determining the sector, the effective voltage vectors at the boundaries of the sector can be identified. To further filter the voltage vectors, a voltage selection method based on the magnitude of the reference voltage vector is proposed. The region can be determined by evaluating the magnitude of the reference voltage vector, as shown in (9). The calculation formula for the reference voltage magnitude is as follows: $\left|u^{ref}\right| = \sqrt{\left(u_d^{ref}\right)^2 + \left(u_q^{ref}\right)^2}$

$$\begin{cases} \text{Region 1, } 0 < \left|u^{ref}\right| \le \frac{2\sqrt{3}}{9}u_{dc} \\ \text{Region 2, } \frac{2\sqrt{3}}{9}u_{dc} < \left|u^{ref}\right| \le \frac{4\sqrt{3}}{9}u_{dc} \\ \text{Region 3, } \frac{4\sqrt{3}}{9}u_{dc} < \left|u^{ref}\right| \le \frac{2\sqrt{3}}{9}u_{dc} \end{cases} \tag{9}$$

By combining the simplified sector determination principle and the magnitude judgment principle, the number of voltage vectors that need to be evaluated within one cycle is significantly reduced—from the original 38 voltage vectors to a maximum of 4. The voltage vector selection is based on the position and magnitude of the reference voltage vector, with the selected voltage vectors being the ones closest to the reference. These vectors are the most likely to be optimal. Therefore, the method ensures that critical voltage vectors are

not lost during the selection process, preventing any deterioration in control performance. This approach greatly balances steady-state performance with computational complexity.

4. Zero-Sequence Current Suppression Strategy

As mentioned earlier, due to the topology of the TPSW-PMSM drive, the emergence of a zero-sequence subspace is inevitable. Section 3 discussed the voltage vector optimization strategy in the $\alpha\beta$ plane, and this section focuses on suppressing the zero-sequence component. First, the vectors within the zero-sequence subspace are analyzed, defining the intersection of the $\alpha\beta$ plane and the z-axis as the zero point of the z-axis, with the positive direction upward and the negative direction downward. The eight voltage vectors within the zero-sequence subspace can be categorized into vectors with positive zero-sequence components ($V_8, V_{10}, V_{12}, V_{14}$), with z-axis components $u_{dc}/3$, and vectors with negative zero-sequence components (V_1, V_3, V_5, V_7), with z-axis components $-u_{dc}/3$. Notably, each of the positive and negative sets includes three fully symmetrical voltage vectors (V_8, V_{12}, V_{14}) and (V_1, V_3, V_7), which implies that their resultant voltage vector can precisely form a complete zero-sequence vector. The set details are shown in Figure 5.

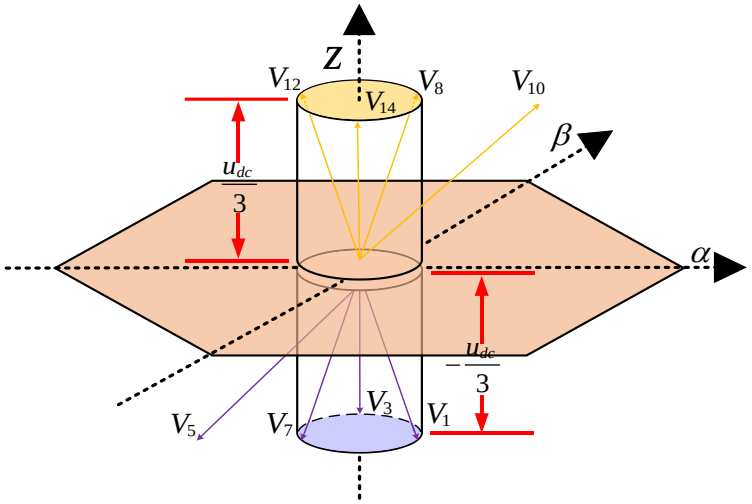

Figure 5. Voltage vector distribution within the zero-sequence subspace.

It can be observed that, due to the symmetry among the three vectors, their resultant vector has no $\alpha\beta$ components and can be modulated independently. Referring to Table 1, to achieve the forward synthesized voltage vector u_{zp}, the conduction times of the four bridge arms are, respectively, defined as follows:

$$(L_1, L_2, L_3, L_4) = k \times (1, \frac{1}{2}, \frac{1}{3}, 0) \times T_s, (0 < k \leq 1)$$

Similarly, to achieve the negative synthesized voltage vector u_{zn}, the conduction times of the four bridge arms are defined as follows.

$$(L_1, L_2, L_3, L_4) = k \times (0, \frac{1}{3}, \frac{1}{2}, 1) \times T_s, (0 < k \leq 1_s)$$

The coefficients k are obtained from (10).

$$\begin{cases} u_0^{ref} = R_s i_0(k) + \frac{L_0[i_0^{ref} - i_0(k)]}{T_s} - 3\omega_e(k)\psi_{f3}\sin(3\theta_e) \\ k = \frac{\sqrt{(u_0^{ref})^2}}{u_{dc}/3} \end{cases} \tag{10}$$

Combining the voltage output strategy on the $\alpha\beta$ plane mentioned in Section 3, the vector modulation in three-dimensional space is completed. However, it is necessary to consider the possibility of over-modulation when zero-sequence voltage is included. Over-modulation refers to a situation in MPC where the amplitude of the generated modulation signal exceeds the allowed maximum range, causing the output voltage to surpass the system's normal operating limits.

If the operating time of any switching signal for the final output voltage vector exceeds T_s, the inverter cannot output that voltage vector, potentially leading to poorer performance. Therefore, it is important to determine the priority between the voltage vector on the $\alpha\beta$ plane and the zero-sequence voltage vector. From the perspective of coverage, the area that the $\alpha\beta$ plane can cover is evidently broader. Thus, when over-modulation occurs, the coefficient k needs to be reconsidered, as shown in (11), where $T_{\alpha\beta}$ represents the conduction time of the bridge arm corresponding to the voltage vector within the $\alpha\beta$ plane. Figure 6 shows the control block diagram of the proposed method. First, the reference voltage value is calculated based on the current reference and the actual current values. Then, the region is selected according to the magnitude of the reference voltage, and the sector is selected based on the position of the reference voltage in the coordinate system. Further, the range of candidate voltage vectors is reduced according to two selection principles. Finally, zero-sequence current suppression is performed.

$$k = \begin{cases} 1 - \max(\frac{T_{\alpha\beta}}{T_s}), & k + \max(\frac{T_{\alpha\beta}}{T_s}) > 1 \\ k, & k + \max(\frac{T_{\alpha\beta}}{T_s}) \leq 1 \end{cases} \tag{11}$$

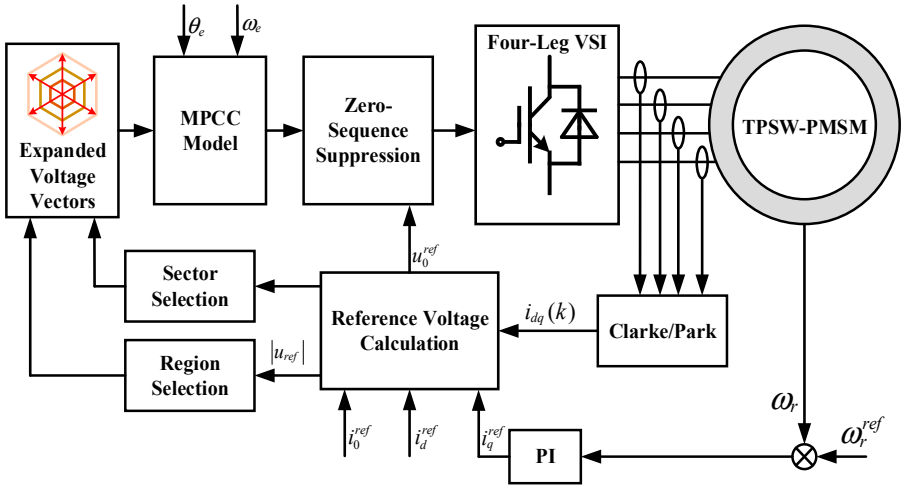

Figure 6. Control diagram of proposed MPCC.

5. Experiment and Discussion

To verify the effectiveness of the proposed method, a simulation model for TPSW-PMSM was built in MATLAB/Simulink, including the conventional MPCC simulation model, the DCC-MPCC simulation model, the DV-MPCC simulation model, and the MPCC simulation model proposed in this paper. Comparative simulation experiments were conducted. Table 3 presents the various parameters used in the simulation models. The conventional Y-connected motor opens the neutral point and connects the three-phase windings of the motor stator in series to form the SW-PMSM.

Table 3. Key parameters of TPSW-PMSM in the simulation model.

Parameters	Value
Stator Resistance (Ω)	0.9
Pole Pairs	4
$d-$ axis Inductance (mH)	3.7
$q-$ axis Inductance (mH)	5
Zero − Sequence Inductance (mH)	4
Flux Linkage (Wb)	0.08
Third Rotor Flux Linkage (Wb)	0.002

5.1. Steady-State Performance and Computational Complexity Evaluation

To fully demonstrate the improvement in steady-state performance achieved by this method, comparative static performance experiments were conducted under different operating conditions. First, the waveforms of the three-phase currents, their THD, and the zero-sequence currents under different control methods at the same rotational speed are presented, as shown in Figures 7 and 8.

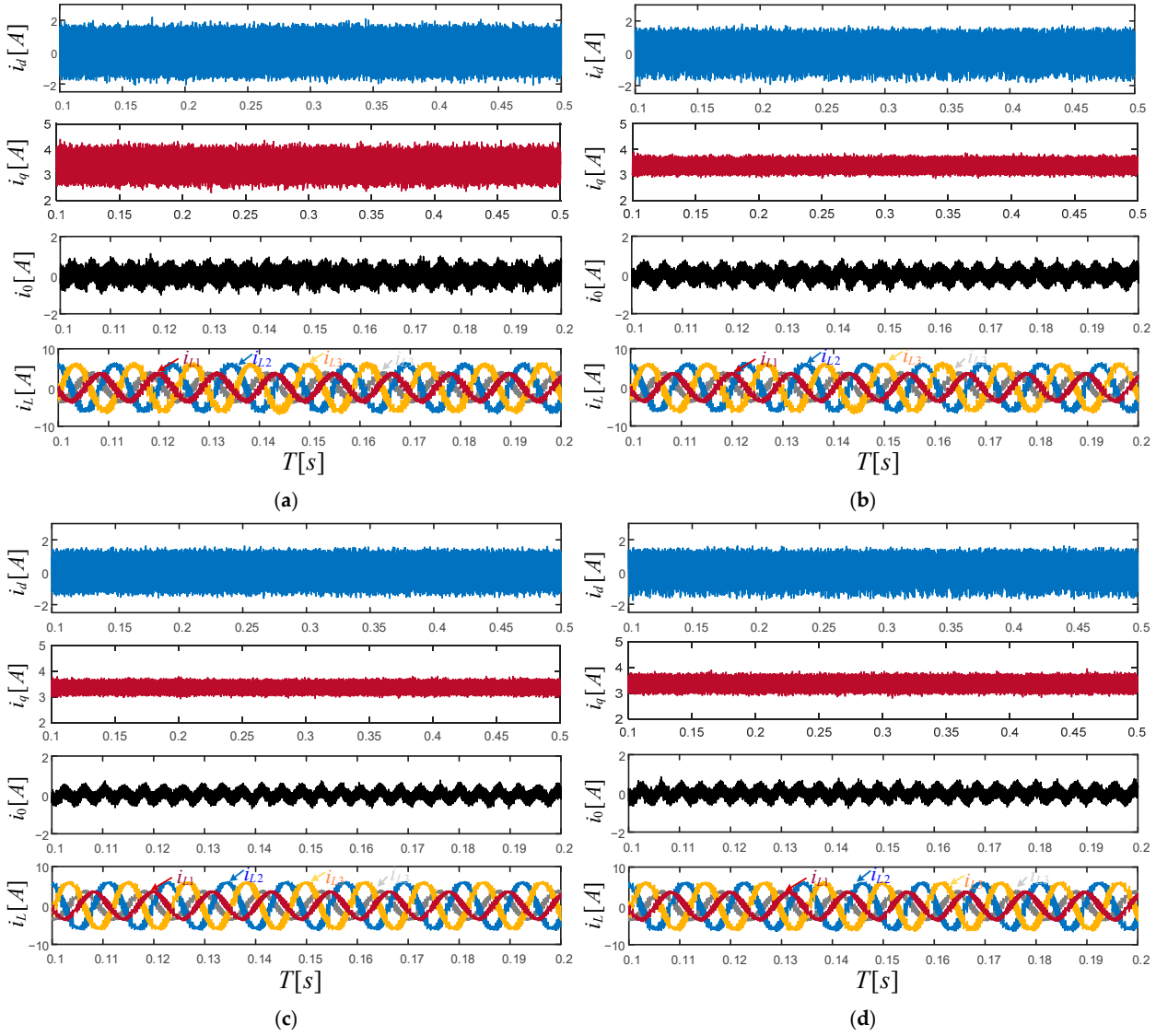

Figure 7. Steady-state current performance under 1000 r/min and 2 N·m conditions: (**a**) conventional MPCC method; (**b**) DCC-MPCC method; (**c**) DV-MPCC method; (**d**) proposed MPCC method.

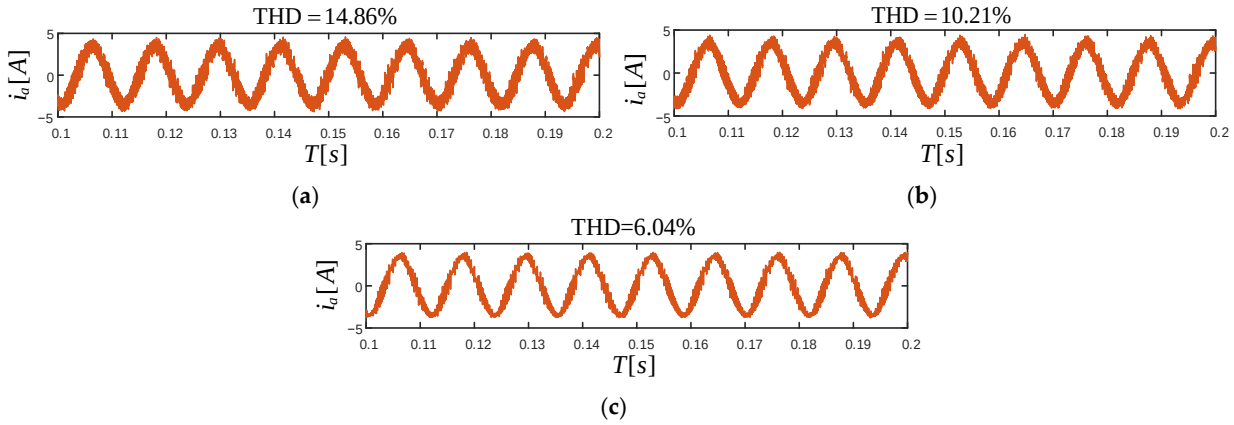

Figure 8. THD of phase current under 1000 r/min and 2 N·m conditions: (**a**) conventional MPCC method; (**b**) DCC-MPCC method; (**c**) proposed MPCC method.

Figure 7 illustrates the waveforms of the *dq*-axis currents and zero-sequence currents under four different control methods, operating at 1000 r/min and 2 N·m. By comparing Figure 7a,b, it is evident that the DCC-MPCC method, which employs a combination of null voltage vectors and active voltage vectors within one control cycle, provides greater flexibility in the amplitude of the output voltage vector. This results in noticeable improvements in both the *dq*-axis currents and the zero-sequence current. Comparing Figure 7a,b,d, the increased number of voltage vectors in the proposed method further expands the feasible range of voltage vectors. As a result, the proposed method demonstrates significant improvements in static performance, evident in both the *dq*-axis currents and the zero-sequence current. Furthermore, a comparison of Figure 7c,d shows that the static performance of the proposed MPCC strategy is comparable to that of the DV-MPCC strategy. This further proves that the proposed method can maintain excellent control performance while significantly reducing computational complexity. The comparison of computational efficiency between the proposed method and the DV-MPCC strategy is detailed in Table 4.

Table 4. Comparison between different methods.

Control Scheme	Number of Candidate Voltage Vectors	Computational Burden of Sector Selection	Time Allocation Calculations
Conventional-MPCC	16	Low	No
DCC-MPCC (no sector selection)	6	Low	Yes
DCC-MPCC (sector selection)	1	High	Yes
DV-MPCC (no sector selection)	$C_8^2 = 28$	Low	Yes
DV-MPCC (sector selection)	1	High	Yes
Proposed MPCC	≤ 4	Low	No

To further quantify the improvement in static performance, the ripple values corresponding to different control strategies were calculated using the standard deviation method. The formula for calculating the *d*-axis current ripple is as follows:

$$i_{dq_rip} = \sqrt{\sum_{n=1}^{N} [i_{dq}(n) - i_{dq_av}]^2 / N} \tag{12}$$

The formula for calculating the ripple value of the zero-sequence current is as follows:

$$i_{0_rip} = \sqrt{\sum_{n=1}^{N} [i_0(n) - i_{0_av}]^2 / N} \tag{13}$$

After calculations, the ripple values corresponding to the conventional MPCC are as follows: the *d*-axis current ripple is 1.893 A, the *q*-axis current ripple is 1.121 A, and the zero-sequence current ripple is 0.977 A. Due to the inclusion of null voltage vectors, the ripple values for DCC-MPCC show a reduction, with values of 1.746 A, 0.973 A, and 0.861 A, respectively. A comparison between DV-MPCC and the proposed method reveals minimal differences in static performance. However, the proposed method significantly reduces the computational burden, ensuring the real-time capability of the control system. Specifically, the proposed method achieves a d-axis current ripple of 1.446 A, which represents a 24% improvement compared to conventional MPCC. Similarly, the q-axis current ripple of the proposed method is 0.660 A, offering a 41% improvement over conventional MPCC. Additionally, the zero-sequence current ripple is improved by approximately 40% compared to the conventional approach.

In comparison to the THD of phase currents shown in Figure 8, it is evident that the proposed method significantly improves static performance over the traditional MPCC method, with a reduction of 59.3% in THD. Compared to the DCC-MPCC method, the THD is reduced by 40.8%.

By comparing Figure 9a,b, it can be concluded that the zero-sequence current suppression method proposed in this paper is effective. The THD is improved by 68.0% compared to the control method without zero-sequence current suppression.

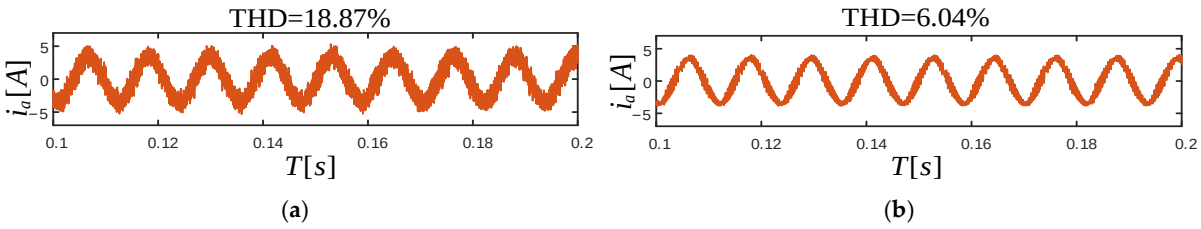

Figure 9. THD of phase current under 1000 r/min and 2 N·m conditions: (**a**) proposed MPCC method without zero-sequence current suppression; (**b**) proposed MPCC method with zero-sequence current suppression.

Table 4 presents a comparison of different methods. The second column lists the number of candidate voltage vectors that need to be traversed in each sampling period. It can be seen that the method proposed in this paper requires traversing at most four voltage vectors per sampling period. Compared to the conventional MPCC, this method significantly reduces the computational burden while greatly improving static performance. In contrast to the DV-MPCC without sector selection, the number of voltage vectors to be traversed per period is reduced by at least 85.7%, which undoubtedly reduces the computational load of the system. Compared to the DV-MPCC with sector selection, the proposed method adopts a simpler and faster sector selection strategy, effectively reducing computation time. Moreover, the method successfully avoids time allocation calculation, further enhancing computational efficiency.

To gain a deeper understanding of the computational complexity of different methods, this paper provides an algorithmic complexity analysis of several model predictive current control (MPCC) strategies:

(1) Conventional MPCC: In conventional single-vector model predictive control, the basic voltage vectors are not processed. In other words, each switching state corresponds to a single, fixed voltage vector. Therefore, the control set consists of 16 elements $\{V_i | i = 0, 1, \ldots, 15\}$, and conventional MPCC is relatively simple and direct, requiring 15 current predictions and 15 cost function evaluations per sampling period.

(2) DCC-MPCC: In DCC-MPCC, a zero-voltage vector is introduced into the sampling period. When considering only voltage vectors in the $\alpha\beta$ plane, this method requires six current predictions and six cost function evaluations per sampling period. If three-dimensional modulation is considered, the computational demand will be even higher.

(3) DV-MPCC:DV-MPCC expands the candidate voltage vectors from the DCC-MPCC approach, allowing the second voltage vector to extend beyond the zero vector. This improves performance but results in an exponential increase in computational load. When considering only the $\alpha\beta$ plane, each sampling period requires $C_8^2 = 28$ current predictions and the same number of cost function evaluations, significantly increasing the computational burden on the control system.

(4) Proposed Method: By utilizing the voltage selection strategy and zero-sequence voltage suppression, this method requires at most four current predictions and four cost function evaluations per sampling period. Compared to conventional MPCC, DCC-MPCC, and DV-MPCC, the computational load per cycle is significantly reduced.

5.2. Dynamic Performance Evaluation

In addition to the steady-state performance evaluation, dynamic performance validation was also conducted. In Figure 10, with torque held constant at 2 N·m, the speed changes from 500 r/min to 1000 r/min. It can be observed that all four methods respond quickly to the speed change, reaching the reference speed within approximately 30 ms. In Figure 11, with the speed maintained at 1000 r/min, the torque is increased from 1 N·m to 2 N·m. Similarly, all four methods exhibit reasonable dynamic performance, with the proposed method showing superior torque ripple suppression compared to conventional methods, demonstrating its advantages.

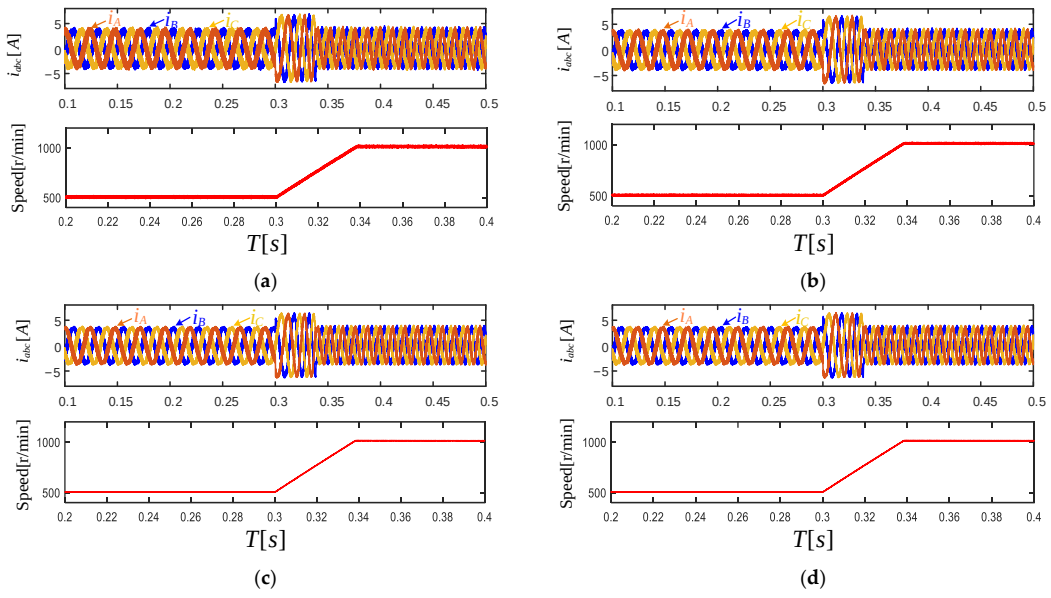

Figure 10. Dynamic performance under a sudden speed change (from 500 r/min to 1000 r/min) at 0.3 s: (**a**) conventional MPCC method; (**b**) DCC-MPCC method; (**c**) DV-MPCC method; (**d**) proposed MPCC method.

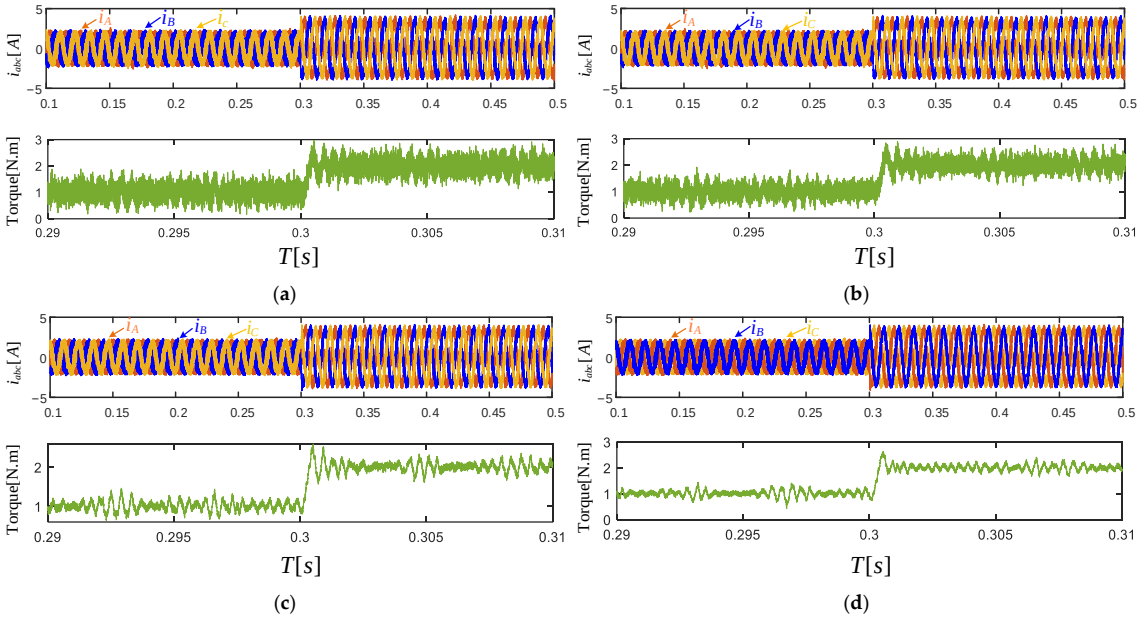

Figure 11. Dynamic performance under a sudden torque change (from 1 N·m to 2 N·m) at 0.3 s: (**a**) conventional MPCC method; (**b**) DCC-MPCC method; (**c**) DV-MPCC method; (**d**) proposed MPCC method.

6. Conclusions

This paper presents an advanced control method for the TPSW-PMSM drive that strikes an optimal balance between computational complexity and static performance while effectively suppressing zero-sequence current to minimize current and torque fluctuations. The proposed method's feasibility in reducing computational load and enhancing static performance is confirmed through simulation studies. The main contributions of this approach include the following:

(1) This paper first addresses the drawbacks of conventional MPCC, which outputs only one voltage vector per cycle, leading to significant errors. To resolve this, the method subdivides basic voltage vectors by their magnitudes and synthesizes additional vectors with greater flexibility in both angle and magnitude. This increases the number of candidate voltage vectors on the 2D plane from 8 to 38, substantially enhancing static performance. Compared to MV-MPCC, this method eliminates the need for calculating the distribution of dwell time, further reducing the computational burden.

(2) Given the potential computational challenges posed by the increased number of voltage vectors, a simplified sector selection scheme and a region selection principle are introduced. These strategies reduce the number of candidate voltage vectors from 38 to a maximum of 4, significantly lowering the computational load.

(3) To mitigate the adverse effects of zero-sequence components on control performance, this paper employs a three-vector synthesis method, effectively suppressing the zero-sequence current and greatly enhancing overall control performance.

Although the results presented in this paper are promising, there are several areas for further improvement: A secondary optimization strategy can be incorporated to refine the first optimal voltage vector, bringing it closer to the reference voltage vector. This approach has already been validated in two-dimensional modulation, and future work will focus on extending this secondary optimization control algorithm to three-dimensional modulation. Extensive experimental validation will be conducted to compare the performance of different control methods, ensuring a comprehensive evaluation. The robustness of the

proposed method will be tested by assessing its performance under parameter variations, providing insights into its practical applicability.

Author Contributions: Conceptualization, J.H.; Data Curation Z.F. (Zhaoyang Fu) and S.W.; Formal Analysis, J.H. and R.X.; Funding Acquisition, Z.F. (Zhaoyang Fu) and S.W.; Investigation, J.H. and Z.F. (Zhengyang Feng); Methodology, J.H., Z.F. (Zhaoyang Fu) and R.X.; Project Administration, Z.F. (Zhaoyang Fu) and S.W.; Software, J.H.; Supervision, Z.F. (Zhaoyang Fu), R.X. and T.J.; Validation, J.H., T.J. and S.W.; Visualization, J.H.; Writing—Original Draft, J.H. and S.W.; Writing—Review & Editing, Z.F. (Zhaoyang Fu), R.X., T.J. and S.W. All authors have read and agreed to the published version of the manuscript.

Funding: This research was funded by the National Key Research and Development Program 2023YFF0719100 and National Natural Science Foundation of China 52477063. The work was partially contributed by the Innovate UK KTP project 10019075.

Data Availability Statement: Data are contained within the article.

Conflicts of Interest: Author Zhengyang Feng was employed by the company Toshiba Europe Ltd. The remaining authors declare that the research was conducted in the absence of any commercial or financial relationships that could be construed as a potential conflict of interest.

References

1. Liu, C. Emerging Electric Machines and Drives-An Overview. *IEEE Trans. Energy Convers.* **2018**, *33*, 2270–2280. [CrossRef]
2. Wang, X.; Wang, D.; Peng, C.; Wang, B.; Wang, X. Torsional Vibration Analysis and Suppression of Interior Permanent Magnet Synchronous Motor with Staggered Segmented Rotor for Electric Vehicles. *IEEE Trans. Transp. Electrif.* **2024**, *10*, 6285–6294. [CrossRef]
3. Lemma, B.D.; Pradabane, S. An Optimized Alternative Fixed Switching 12-Sector Space Vector Pulse Width Modulation Control of Open-End Winding PMSM Drive. *IEEE Access* **2023**, *11*, 55169–55177. [CrossRef]
4. Wang, X.; Lin, X.; Huang, Q.; Xie, W. An Improved Parallel Predictive Torque Control for Permanent Magnet Synchronous Motor. *IEEE Access* **2023**, *11*, 32496–32507. [CrossRef]
5. Bao, G.; Qi, W.; He, T. Direct Torque Control of PMSM with Modified Finite Set Model Predictive Control. *Energies* **2020**, *13*, 234. [CrossRef]
6. Sun, X.; Liu, Z.; Li, A.; Wang, Z.; Jiang, D.; Qu, R. Self-Adaptive Fault-Tolerant Control of Three-Phase Series-End Winding Motor Drive. *IEEE Trans. Power Electron.* **2022**, *37*, 10939–10950. [CrossRef]
7. Zuo, Y.; Zhu, X.; Lee, C.H.T. Fault-Tolerant Control for Multiple Open-Leg Faults in Open-End Winding Permanent Magnet Synchronous Motor System Based on Winding Reconnection. *IEEE Trans. Power Electron.* **2021**, *36*, 6068–6078. [CrossRef]
8. Dong, Y.; Zhang, S.; Zhang, C.; Wang, S. A Parameter Robust Fault-Tolerant Control Scheme for Open-Winding Permanent Magnet Synchronous Motors in Flux-Weakening Regions. *IEEE J. Emerg. Sel. Top. Power Electron.* **2024**, *12*, 4191–4203. [CrossRef]
9. Lee, H.W.; Lee, K.B. Open-fault diagnosis and tolerant control of a dual inverter fed open-end winding interior permanent magnet synchronous motor. *J. Power Electron.* **2024**, *24*, 1071–1080. [CrossRef]
10. Bao, Y.; Zhang, X.; Zhao, J.; Li, B.; Xu, C. Research of Fault-Tolerant Control Strategy for Open-End Winding PMSM Under Open-Phase Fault. In Proceedings of the 2023 IEEE PELS Students and Young Professionals Symposium (SYPS), Shanghai, China, 27–29 August 2023; pp. 1–5.
11. Oto, Y.; Noguchi, T.; Fauziah, M.B. Experimental Verification of Fault Tolerant Operation Focusing on DC-Bus Battery Failure in Dual Inverter Motor Drive. *World Electr. Veh. J.* **2019**, *10*, 65. [CrossRef]
12. Li, A.; Jiang, D.; Liu, Z.; Sun, X. Generalized PWM Method for Series-End Winding Motor Drive. *IEEE Trans. Power Electron.* **2021**, *36*, 4452–4462. [CrossRef]
13. Dong, Z.; Liu, C.; Song, Z.; Liu, S. Suppression of Dual-Harmonic Components for Five-Phase Series-Winding PMSM. *IEEE Trans. Transp. Electrif.* **2022**, *8*, 121–134. [CrossRef]
14. Tolbert, L.M.; Peng, F.Z.; Habetler, T.G. Multilevel inverters for electric vehicle applications. In Proceedings of the Power Electronics in Transportation (Cat. No. 98TH8349), Dearborn, MI, USA, 22–23 October 1998; pp. 79–84.
15. Oliveira, A.C.; Jacobina, C.B.; Lima, A.M.N. Improved Dead-Time Compensation for Sinusoidal PWM Inverters Operating at High Switching Frequencies. *IEEE Trans. Ind. Electron.* **2007**, *54*, 2295–2304. [CrossRef]
16. Hu, W.; Ruan, C.; Nian, H.; Sun, D. Zero-Sequence Current Suppression Strategy with Common-Mode Voltage Control for Open-End Winding PMSM Drives with Common DC Bus. *IEEE Trans. Ind. Electron.* **2021**, *68*, 4691–4702. [CrossRef]

17. Song, Z.; Dong, Z.; Wang, W.; Liu, S.; Liu, C. A Novel Modulation Strategy for Asymmetrical Six-Phase Series-Winding PMSM Based on Predictive Controller. *IEEE Trans. Ind. Electron.* **2023**, *70*, 5592–5603. [CrossRef]
18. Xu, Y.; Morito, C.; Lorenz, R.D. Extending High-Speed Operating Range of Induction Machine Drives Using Deadbeat-Direct Torque and Flux Control With Precise Flux Weakening. *IEEE Trans. Ind. Appl.* **2019**, *55*, 3770–3780. [CrossRef]
19. Kubo, H.; Yamamoto, Y.; Kondo, T.; Rajashekara, K.; Zhu, B. Zero-sequence current suppression for open-end winding induction motor drive with resonant controller. In Proceedings of the 2016 IEEE Applied Power Electronics Conference and Exposition (APEC), Long Beach, CA, USA, 20-24 March 2016; pp. 2788–2793.
20. Cui, R.; Fan, Y.; Cheng, M. A New Zero-Sequence Current Suppression Control Strategy for Five-Phase Open-Winding Fault-Tolerant Fractional-Slot Concentrated Winding IPM Motor Driving System. *IEEE Trans. Ind. Appl.* **2019**, *55*, 2731–2740. [CrossRef]
21. Lu, Q.; Zuo, Y.; Zhang, T.; Mo, L. Zero-Sequence Current Suppression for Open-Winding Permanent Magnet Brushless Motor Driving System Based on Second Order Generalized Integrator. *IEEE Access* **2020**, *8*, 37465–37473. [CrossRef]
22. Su, Z.; Zuo, Y.; Lin, X. Direct Torque Control for Series-Winding PMSM with Zero-Sequence Current Suppression Capability. *Electronics* **2023**, *12*, 4692. [CrossRef]
23. Hu, W.; Nian, H.; Zheng, T. Torque Ripple Suppression Method with Reduced Switching Frequency for Open-Winding PMSM Drives with Common DC Bus. *IEEE Trans. Ind. Electron.* **2019**, *66*, 674–684. [CrossRef]
24. Dong, Z.; Chen, Y.; Feng, K.; Liu, C. Multivector-Based Model Predictive Current Control with Zero-Sequence Current Suppression for Three-Phase Series-End Winding Permanent Magnet Synchronous Motor Drives. *IEEE Trans. Transp. Electrif.* **2023**, *9*, 3282–3294. [CrossRef]
25. Rodriguez, J.; Garcia, C.; Mora, A.; Flores-Bahamonde, F.; Acuna, P.; Novak, M.; Zhang, Y.; Tarisciotti, L.; Davari, S.A.; Zhang, Z.; et al. Latest Advances of Model Predictive Control in Electrical Drives-Part I: Basic Concepts and Advanced Strategies. *IEEE Trans. Power Electron.* **2022**, *37*, 3927–3942. [CrossRef]
26. Sun, X.; Li, T.; Yao, M.; Lei, G.; Guo, Y.; Zhu, J. Improved Finite-Control-Set Model Predictive Control with Virtual Vectors for PMSHM Drives. *IEEE Trans. Energy Convers.* **2022**, *37*, 1885–1894. [CrossRef]
27. Yu, F.; Liu, X.; Zhu, Z.; Mao, J. An Improved Finite-Control-Set Model Predictive Flux Control for Asymmetrical Six-Phase PMSMs with a Novel Duty-Cycle Regulation Strategy. *IEEE Trans. Energy Convers.* **2021**, *36*, 1289–1299. [CrossRef]
28. Zhou, Y.; Li, H.; Liu, R.; Mao, J. Continuous Voltage Vector Model-Free Predictive Current Control of Surface Mounted Permanent Magnet Synchronous Motor. *IEEE Trans. Energy Convers.* **2019**, *34*, 899–908. [CrossRef]
29. Wang, F.; He, L.; Rodriguez, J. FPGA-Based Continuous Control Set Model Predictive Current Control for PMSM System Using Multistep Error Tracking Technique. *IEEE Trans. Power Electron.* **2020**, *35*, 13455–13464. [CrossRef]
30. Wróbel, K.; Serkies, P.; Szabat, K. Continuous and Finite Set Model Predictive Control of Induction Motor Drive. In Proceedings of the IECON 2019—45th Annual Conference of the IEEE Industrial Electronics Society, Lisbon, Portugal, 14–17 October 2019; pp. 963–968.
31. Ahmed, A.A.; Koh, B.K.; Lee, Y.I. A Comparison of Finite Control Set and Continuous Control Set Model Predictive Control Schemes for Speed Control of Induction Motors. *IEEE Trans. Ind. Inform.* **2018**, *14*, 1334–1346. [CrossRef]
32. Yang, H.; Wu, H. Summary of Model Predictive Control Methods in Motor Drive System. In Proceedings of the 2021 IEEE 7th International Conference on Control Science and Systems Engineering (ICCSSE), Qingdao, China, 30 July–1 August 2021; pp. 169–174.
33. Zhao, K.; Zhou, R.; She, J.; Zhang, C.; He, J.; Li, X. A Model Predictive Current Control Based on Sliding Mode Speed Controller for PMSM. In Proceedings of the 2020 13th International Conference on Human System Interaction (HSI), Tokyo, Japan, 6–8 June 2020; pp. 229–233.
34. Sun, X.; Wu, M.; Lei, G.; Guo, Y.; Zhu, J. An Improved Model Predictive Current Control for PMSM Drives Based on Current Track Circle. *IEEE Trans. Ind. Electron.* **2021**, *68*, 3782–3793. [CrossRef]
35. Kumar, P.D.; Ramesh, T.; Pothuraju, R. Model Predictive Current Control for Multi-Level Inverter fed Speed Sensorless PMSM Drive. In Proceedings of the 2022 IEEE IAS Global Conference on Emerging Technologies (GlobConET), Arad, Romania, 20–22 May 2022; pp. 375–380.
36. Dang, C.; Dou, M.; Wang, Y. Model Predictive Direct Torque Control for PMSM Drives in M–T Frame. In Proceedings of the 2021 IEEE International Conference on Predictive Control of Electrical Drives and Power Electronics (PRECEDE), Jinan, China, 20–22 November 2021; pp. 138–141.
37. Ma, C.; Yao, X.; Li, H.; Belie, F.D. Current Boundary Based Model Predictive torque control of PMSM. In Proceedings of the 2019 22nd International Conference on Electrical Machines and Systems (ICEMS), Harbin, China, 1–14 August 2019; pp. 1–6.
38. Mao, H.; Tang, X.; Tang, H. Speed control of PMSM based on neural network model predictive control. *Trans. Inst. Meas. Control* **2022**, *44*, 2781–2794. [CrossRef]
39. Hassan, A.A.; Kassem, A.M. Modeling, Simulation and Performance Improvements of a PMSM Based on Functional Model Predictive Control. *Arab. J. Sci. Eng.* **2013**, *38*, 3071–3079. [CrossRef]

40. Zhang, Y.; Bai, Y.; Yang, H. A Universal Multiple-Vector-Based Model Predictive Control of Induction Motor Drives. *IEEE Trans. Power Electron.* **2018**, *33*, 6957–6969. [CrossRef]
41. Zhang, Y.; Jiang, H.; Yang, H. Model Predictive Control of PMSM Drives Based on General Discrete Space Vector Modulation. *IEEE Trans. Energy Convers.* **2021**, *36*, 1300–1307. [CrossRef]
42. Zhang, Y.; Xu, D.; Huang, L. Generalized Multiple-Vector-Based Model Predictive Control for PMSM Drives. *IEEE Trans. Ind. Electron.* **2018**, *65*, 9356–9366. [CrossRef]

Disclaimer/Publisher's Note: The statements, opinions and data contained in all publications are solely those of the individual author(s) and contributor(s) and not of MDPI and/or the editor(s). MDPI and/or the editor(s) disclaim responsibility for any injury to people or property resulting from any ideas, methods, instructions or products referred to in the content.